



## Measuring the scattering coefficient of turbid media from two-photon microscopy

David Sevrain, Matthieu Dubreuil, Aymeric Leray, Christophe Odin, Yann Le Grand

### ► To cite this version:

David Sevrain, Matthieu Dubreuil, Aymeric Leray, Christophe Odin, Yann Le Grand. Measuring the scattering coefficient of turbid media from two-photon microscopy. *Optics Express*, 2013, 21 (21), pp.25221. 10.1364/OE.21.025221 . hal-00907898

**HAL Id: hal-00907898**

**<https://hal.univ-brest.fr/hal-00907898>**

Submitted on 22 Nov 2013

**HAL** is a multi-disciplinary open access archive for the deposit and dissemination of scientific research documents, whether they are published or not. The documents may come from teaching and research institutions in France or abroad, or from public or private research centers.

L'archive ouverte pluridisciplinaire **HAL**, est destinée au dépôt et à la diffusion de documents scientifiques de niveau recherche, publiés ou non, émanant des établissements d'enseignement et de recherche français ou étrangers, des laboratoires publics ou privés.

# Measuring the scattering coefficient of turbid media from two-photon microscopy

David Sevrain,<sup>1</sup> Matthieu Dubreuil,<sup>1</sup> Aymeric Leray,<sup>2,3</sup> Christophe Odin,<sup>3</sup>  
and Yann Le Grand<sup>1,\*</sup>

<sup>1</sup> Université de Brest, EA 938 Laboratoire de Spectrométrie et Optique Laser (LSOL), SFR ScInBioS, 29238 Brest Cedex 3, France

<sup>2</sup> Université de Lille-Nord de France, USR CNRS 3078 Institut de Recherche Interdisciplinaire (IRI), 59650 Villeneuve d'Ascq, France

<sup>3</sup> Université de Rennes 1, URI/UMR CNRS 6251 Institut de Physique de Rennes (IPR), 35042 Rennes Cedex France  
[\\*yann.legrand@univ-brest.fr](mailto:yann.legrand@univ-brest.fr)

**Abstract:** In this paper, we propose a new and simple method based on two-photon excitation fluorescence (TPEF) microscopy to measure the scattering coefficient  $\mu_s$  of thick turbid media. We show, from Monte Carlo simulations, that  $\mu_s$  can be derived from the axial profile of the ratio of the TPEF signals epi-collected by the confocal and the non-descanned ports of a scanning microscope, independently of the anisotropy factor  $g$  and of the absorption coefficient  $\mu_a$  of the medium. The method is validated experimentally on tissue-mimicking optical phantoms, and is shown to have potential for imaging the scattering coefficient of heterogeneous media.

©2013 Optical Society of America

**OCIS codes:** (180.4315) Nonlinear microscopy; (180.1790) Confocal microscopy; (290.7050) Turbid media; (290.5820) Scattering measurements; (170.6935) Tissue characterization; (170.3660) Light propagation in tissues.

---

## References and links

1. V. V. Tuchin, "Light scattering study of tissues," *Phys.-Usp.* **40**(5), 495–515 (1997).
2. V. V. Tuchin, *Handbook of Biomedical Diagnostics*, **PM107** (SPIE Press, 2002).
3. L.-V. Wang and H. Wu, *Biomedical Optics, Principles and Imaging* (Wiley Inter-Science 2007).
4. S. L. Jacques, B. Wang, and R. Samatham, "Reflectance confocal microscopy of optical phantoms," *Biomed. Opt. Express* **3**(6), 1162–1172 (2012).
5. W. Denk, J. H. Strickler, and W. W. Webb, "Two-photon laser scanning fluorescence microscopy," *Science* **248**(4951), 73–76 (1990).
6. A. Leray, C. Odin, E. Huguet, F. Amblard, and Y. Le Grand, "Spatially distributed two-photon excitation fluorescence in scattering media: Experiments and time-resolved Monte Carlo simulations," *Opt. Commun.* **272**(1), 269–278 (2007).
7. Y. Le Grand, A. Leray, T. Guilbert, and C. Odin, "Non-descanned versus descanned epifluorescence collection in two-photon microscopy: Experiments and Monte Carlo simulations," *Opt. Commun.* **281**(21), 5480–5486 (2008).
8. E. Beaurepaire and J. Mertz, "Epifluorescence collection in two-photon microscopy," *Appl. Opt.* **41**(25), 5376–5382 (2002).
9. H. Szmajcinski, I. Gryczynski, and J. R. Lakowicz, "Spatially localized ballistic two-photon excitation in scattering media," *Biospectroscopy* **4**(5), 303–310 (1998).
10. A. Leray, C. Odin, and Y. Le Grand, "Out-of-focus fluorescence collection in two-photon microscopy of scattering media," *Opt. Commun.* **281**(24), 6139–6144 (2008).
11. S. L. Jacques, "Light distributions from point, line and plane sources for photochemical reactions and fluorescence in turbid biological tissues," *Photochem. Photobiol.* **67**(1), 23–32 (1998).
12. W. R. Zipfel, R. M. Williams, and W. W. Webb, "Nonlinear magic: multiphoton microscopy in the biosciences," *Nat. Biotechnol.* **21**(11), 1369–1377 (2003).
13. G. Marsaglia and T. A. Bray, "A Convenient Method for Generating Normal Variables," *SIAM Rev.* **6**(3), 260–264 (1964).
14. N. Ghosh, H. S. Patel, and P. K. Gupta, "Depolarization of light in tissue phantoms - effect of a distribution in the size of scatterers," *Opt. Express* **11**(18), 2198–2205 (2003).
15. L. G. Henyey and J. L. Greenstein, "Diffuse radiation in the galaxy," *Astrophys. J.* **93**, 70–83 (1941).
16. C. Xu, R. M. Williams, W. Zipfel, and W. W. Webb, "Multiphoton excitation cross-sections of molecular fluorophores," *Bioimaging* **4**(3), 198–207 (1996).

17. M. Daimon and A. Masumura, "Measurement of the refractive index of distilled water from the near-infrared region to the ultraviolet region," *Appl. Opt.* **46**(18), 3811–3820 (2007).
18. A. Jain, A. H. J. Yang, and D. Erickson, "Gel-based optical waveguides with live cell encapsulation and integrated microfluidics," *Opt. Lett.* **37**(9), 1472–1474 (2012).
19. S. N. Kasarova, N. G. Sultanova, C. D. Ivanov, and I. D. Nikolov, "Analysis of the dispersion of optical plastic materials," *Opt. Mater.* **29**(11), 1481–1490 (2007).
20. W.-F. Cheong, S. A. Prahl, and A. J. Welch, "A review of the optical properties of biological tissues," *IEEE J. Quantum Electron.* **26**(12), 2166–2185 (1990).

## 1. Introduction

Non-invasive measurement of the optical properties of tissues offers interesting possibilities and perspectives in terms of *in vivo* diagnosis and therapy [1]. For this purpose, the so-called therapeutic window (wavelength range comprised between 0.6 and 1.3  $\mu\text{m}$ ) is generally used to both prevent photodamage and increase penetration depth [2]. As scattering prevails over absorption within this wavelength range, tissues then behave mainly like turbid media. By excluding interfacial, inhomogeneity and polarization effects, such media can be characterized by three optical parameters which are the scattering coefficient  $\mu_s$  (the inverse of the mean free path  $l_s$  between two scattering events), the associated anisotropy factor  $g = \langle \cos\theta \rangle$  (the average cosine of the scattering angle  $\theta$ ) and the absorption coefficient  $\mu_a$  ( $\mu_a \ll \mu_s$  in the relevant wavelength range). Generally, measurement of these parameters *in vivo* or simply within thick samples rules out transmission geometries. Moreover the usual backscattering methods based on the diffusion theory like diffuse reflectance provide a reduced scattering coefficient  $\mu'_s = \mu_s(1-g)$  but fail to separate  $\mu_s$  and  $g$  ([3] and references therein). In order to measure  $\mu_s$  independently of  $g$  within thick samples, it is necessary to consider backward layouts able to select unscattered or ballistic photons to the detriment of scattered ones. In that case,  $\mu_s$  can be derived from an apparent attenuation coefficient obtained by fitting the measured intensity as a function of depth with a Beer-Lambert law. Reflectance confocal laser microscopy has been recently shown to have potential to measure  $\mu_s$  by isolating unscattered light produced by backscattering of a focusing laser beam within the focal volume of an objective lens [4]. However, evaluation of  $\mu_s$  from the measured axial profile of the backscattered intensity detected through a confocal pinhole is highly model-dependent. Indeed, as a high-NA objective lens is used to localize the backscattering source, the extra-path length of photons has to be considered. Modeling the scattering coefficient as a function of the apparent attenuation coefficient then lays on the calculation of a geometrical correcting factor which depends on the expected angular dependence of both excitation and backscattered light. Furthermore, an additional correction depending on the value of  $g$  is necessary; it is obtained empirically using Monte Carlo simulations in order to account for the contribution of the laser photons reaching the focus despite scattering. Finally, the authors have neglected the effect of absorption although the measured attenuation coefficient is modified by both absorption and scattering.

In this paper we propose a new and simple method able to measure  $\mu_s$  independently of  $g$  and  $\mu_a$  within thick turbid media. It is based on two-photon microscopy and circumvents the drawbacks of the reflectance confocal microscopy method listed above. Indeed, by measuring the axial profile of the ratio of the collection efficiencies detected by the confocal and non-descanned ports of a two-photon fluorescence scanning microscope, we demonstrate the possibility of measuring an apparent scattering coefficient, independently of  $\mu_a$ ,  $g$ , and of the microscope excitation function. Moreover, a simple analytical model was developed for recovering with a very good accuracy the true scattering coefficient from the apparent one.

The paper is organized as follows. In Section 2, we present in detail the principle of our method. Then, the results of Monte Carlo simulations of the collection efficiency performed in order to validate our concept are reported in section 3. In section 4, we describe a simple analytical model valid for high-NA objectives, which makes it possible to get back to the true scattering coefficient. Finally, we present in section 5 experimental results from various

scattering biomimetic media made of polystyrene spheres embedded in agarose gel matrices. We show the ability of our technique for discriminating between two different scattering media either superposed or side-by-side.

## 2. Principle of the method

Two-photon excitation fluorescence (TPEF) microscopy takes advantage of the intrinsic localization of nonlinear absorption within the focal volume of the objective lens to image beyond the mean free path  $l_s = \mu_s^{-1}$  of turbid media [5,6]. Robustness to scattering results mainly from the ability to avoid descanned (DS) collection modalities used in confocal microscopy. Indeed, even after removal of the confocal pinhole, DS paths have still low fields of view (FOV) which are inconsistent with efficient collection of scattered light. Wide FOV non-descanned (NDS) pathways are then preferred in TPEF microscopy; they consist in directly reimaging the rear pupil of the objective lens onto an external detector which is set as close as possible to the collecting optics [7,8]. The effective FOV of well-designed NDS setup is then just limited to that of the objective itself. Moreover, by remarking that tissues have generally high  $g$ -values ( $g > 0.8$ ) and using a long working distance objective, the NDS collection efficiency  $\eta_{\text{NDS}}$  was shown to remain almost constant up to an imaging depth  $z_0$  approximately equal to the radius  $r_{\text{fov}}$  of the collecting FOV of the microscope [7,8]. This depth range where  $\eta_{\text{NDS}}$  is almost constant is equal to a few hundreds of microns for high-NA objective lenses used in two-photon microscopy. On the contrary, if absorption is neglected, the collection efficiency  $\eta_{\text{conf}}$  of the confocal path decreases exponentially with  $z_0$ , like the probability for a fluorescence photon not to be scattered before exiting the turbid medium, expressed by  $\exp(-\mu_s^{\text{app}} z_0)$ . Here  $\mu_s^{\text{app}}$  corresponds to an apparent scattering coefficient. Due to the isotropic fluorescence emission,  $\mu_s^{\text{app}}$  can be easily related to the true coefficient  $\mu_s$ , independently of  $g$ , by averaging the Beer-Lambert law over all photon paths within the numerical aperture of the collecting objective, as shown in section 4. Unfortunately, direct measurement of  $\eta_{\text{conf}}$  is not possible because the detected fluorescence signal further depends on the excitation function of the microscope  $f_{\text{exc}}$ . Since TPEF intensity is mainly produced by ballistic laser photons reaching the objective focal volume [9],  $f_{\text{exc}}$  is also expected to decrease exponentially with the imaging depth  $z_0$  as  $\exp(-2\mu_s^{\text{exc}} z_0)$ , where  $\mu_s^{\text{exc}}$  is the scattering coefficient for the excitation wavelength. Moreover  $f_{\text{exc}}$  depends on many parameters like the average laser power  $\bar{P}$ , the pulse width  $\tau$ , the pulse repetition rate  $f$ , the concentration of fluorophores  $C$ , the two-photon cross-section  $\sigma_{\text{TPEF}}$  and the quantum yield  $\Phi$  of the excited fluorophores. However, the TPEF process is independent of the collection modality, whether confocal or non-descanned [10]. The collected fluorescence signal  $F_{\text{coll}}$  is then written as:

$$F_{\text{conf}}^{\text{coll}} = f_{\text{exc}}(\bar{P}, \tau, f, C, \sigma_{\text{TPEF}}, \Phi, \mu_s^{\text{exc}}, z_0) \eta_{\text{conf}} \quad (1.a)$$

for the confocal pathway, and:

$$F_{\text{NDS}}^{\text{coll}} = f_{\text{exc}}(\bar{P}, \tau, f, C, \sigma_{\text{TPEF}}, \Phi, \mu_s^{\text{exc}}, z_0) \eta_{\text{NDS}} \quad (1.b)$$

for the non-descanned pathway. Consequently,  $F_{\text{conf}}^{\text{coll}} / F_{\text{NDS}}^{\text{coll}}$  is independent of the excitation function of the microscope, and since  $\eta_{\text{NDS}}$  is almost constant for shallow depths, it comes:

$$F_{\text{conf}}^{\text{coll}} / F_{\text{NDS}}^{\text{coll}} \propto \eta_{\text{conf}} \approx \exp(-\mu_s^{\text{app}} z_0) \quad (2)$$

Then measuring  $F_{\text{conf}}^{\text{coll}} / F_{\text{NDS}}^{\text{coll}}$  as a function of the imaging depth  $z_0$  provides a robust method to recover the apparent scattering coefficient, which is directly related to the true scattering coefficient. Furthermore, we show in the next section that the absorption by the sample does not contribute significantly to the decay of this ratio.

### 3. Monte Carlo simulations

Our Monte Carlo simulations of  $\eta_{\text{conf}}$  and  $\eta_{\text{NDS}}$  were based on a program developed for modeling photon transport in living tissues [11]. The collection efficiency of the microscope was defined as the ratio of the number of photons collected through the scattering medium with respect to the total number of photons emitted by the fluorescence source. In order to take into account diffraction in the simulation of the collection efficiency  $\eta_{\text{conf}}$  through a confocal pinhole with a finite size, the TPEF source was assumed to be confined in a small focal volume (centered on the geometrical focus of the objective lens) corresponding to the two-photon illumination point-spread function (IPSF<sup>2</sup>) of the microscope [12]. Fluorescence photons were then launched isotropically from this volume (see Fig. 1).

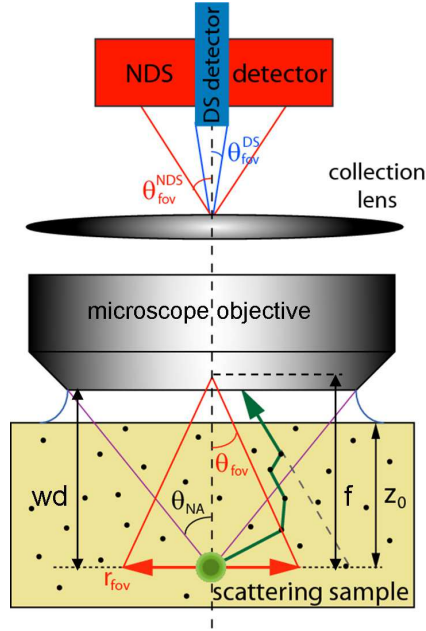


Fig. 1. Geometry of the collection paths used in the Monte Carlo simulations and useful parameters.  $f$ : focal length of the objective;  $wd$ : working distance;  $\theta_{\text{NA}}$ : numerical aperture angle;  $r_{\text{fov}}$ : linear field of view;  $\theta_{\text{fov}}^{\text{DS}}$  and  $\theta_{\text{fov}}^{\text{NDS}}$ : angular field of view of the confocal (or descanned DS) and non-descanned NDS ports, respectively.

The starting coordinates of these photons were sampled as normal random variables using the Marsaglia polar method [13] and a Gaussian probability density determined by the diffraction-limited lateral and axial extents of the IPSF<sup>2</sup> noted respectively  $w_{xy}$  and  $w_z$  [12]. It is worthwhile to note that  $w_{xy}$  and  $w_z$  stand for the 1/e half-widths of the IPSF<sup>2</sup>. To insure good statistics on the number of collected photons, especially when  $\eta_{\text{conf}} \ll 1$  for imaging depths  $z_0 > \mu_s^{-1}$ ,  $N = 5.10^6$  photons were launched from each depth  $z_0$ . Photon propagation within the turbid medium consisted on simple ray-tracing based on geometrical optics, phase and polarization being insignificant in case of forward scattering of incoherent light like fluorescence in tissue-mimicking optical phantoms [14]. The step size 's' between two scattering events and the cosine of the deflection angle were sampled according to probability densities derived from respectively the Beer-Lambert law and the Henyey-Greenstein phase function [15]. Assuming a random number  $\xi$  uniformly distributed over the interval [0,1], standard sampling expressions were then  $s = -\ln(\xi)/\mu_s$  and  $\cos\theta = (1 + g^2 - [(1-g^2)/(1-g + 2g\xi)]^2)/2g$  if  $g \neq 0$  or  $\cos\theta = 2\xi - 1$  if  $g = 0$ . The scattering azimuthal angle  $\psi$  was assumed to be uniformly distributed over  $[0, 2\pi]$ , then sampled as  $\psi = 2\pi\xi$ . The turbid medium was

considered homogeneous. Absorption was accounted by attributing an initial weight of 1 to each launched photon, then multiplying this weight by a factor  $\mu_s/(\mu_s + \mu_a)$  for each scattering event. Since the turbid medium was first considered as semi-infinite and bounded by one exit plane, it was necessary to limit the scattering volume in order to minimize the computation time. Photons were then considered lost beyond a preset distance of typically 10 times the effective mean free path (scattering volume  $\sim 1\text{cm}^3$ ). The exit plane was assumed smooth for not altering photon trajectory. Index matching between the turbid sample and the immersion medium was assumed, thus Fresnel refraction and reflection at this interface were not considered. Once photons escaped from the turbid medium, conditions for epi-collection were two-fold: photons had to hit the objective's front aperture and to enter the FOV of the microscope [7]. Photon trajectories which fulfilled the first condition were retraced back to the focal plane of the objective lens. To account for diffraction at collection, a weight was assigned to each of these photons according to their position with respect to the optical axis. The weighting function was obtained numerically from the convolution of a circular aperture, corresponding to the FOV of the microscope, and a Gaussian function, representing the PSF of the objective at the collection wavelength (i.e. 600nm, see section 5 for details). Note that the FOV of the microscope is proportional to the pinhole diameter for confocal collection (see below for details).

Figure 2 is a semi-log representation of our Monte Carlo simulations of  $\eta_{\text{conf}}/\eta_0$  and  $\eta_{\text{NDS}}/\eta_0$  as a function of the imaging depth  $z_0$ , where  $\eta_0 = (1 - \cos\theta_{\text{NA}})/2$  is the collection efficiency in clear medium of the objective lens of half-angle aperture  $\theta_{\text{NA}}$ . The simulated water immersion ( $n = 1.33$ ) objective lens was a long working distance ( $\text{wd} = 2\text{mm}$ ),  $\text{NA} = 0.9$  ( $\text{NA} = n \cdot \sin\theta_{\text{NA}}$ ) and  $60\times$  magnification model which equipped our microscope. The scattering coefficient of the turbid medium was fixed to  $\mu_s = 100\text{cm}^{-1}$ . Simulations were performed for two absorption coefficients  $\mu_a = 0$  and  $\mu_a = \mu_s/10 = 10\text{cm}^{-1}$  and two anisotropy factors  $g = 0.85$  and  $0.95$ . Moreover,  $\eta_{\text{conf}}$  was calculated for the smallest (#1) and the largest (#4) pinholes of our scanning microscope, whose diameters  $\Phi_p$  are respectively of 60 and  $200\mu\text{m}$ . The corresponding values of the FOV radius  $r_{\text{fov}}$  in the focal plane of the aforementioned  $60\times$  objective lens was found to be  $0.14\mu\text{m}$  for pinhole 1 and  $0.47\mu\text{m}$  for pinhole 4, using the relation  $r_{\text{fov}} = \Phi_p/(2 \times 3.55 \times 60)$ . The factor of 3.55 in this formula stands for the ratio of the focal lengths of the pinhole focusing lens and the scan lens. Note that the  $r_{\text{fov}}$  values bound the lateral extent  $w_{xy} \approx 0.21\mu\text{m}$  of the  $\text{IPSF}^2$  found for a 0.9-NA water-immersion objective lens at the illumination wavelength  $\lambda \approx 830\text{nm}$  of our femtosecond laser. Moreover  $r_{\text{fov}}$  for the NDS collection path was previously measured to be  $320\mu\text{m}$  in the focal plane of the  $60\times$  lens [6]. This explains why the simulations were ended at a depth  $z_0 = 300\mu\text{m}$ . In fact,  $\eta_{\text{NDS}}$  is almost constant for  $\mu_a = 0$  (see Fig. 2) within this depth range.

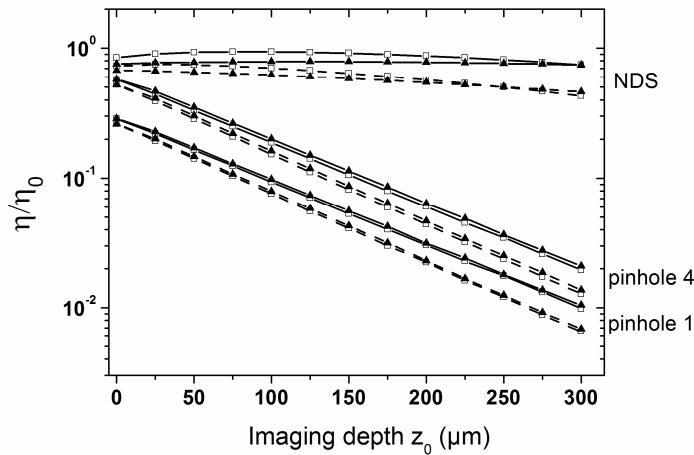


Fig. 2. Monte Carlo simulations of the z-profile of collection efficiencies  $\eta_{\text{conf}}$  (pinhole 1 and 4) and  $\eta_{\text{NDS}}$ , without absorption (full lines) and with absorption  $\mu_a = 10\text{cm}^{-1}$  (dashed lines), for  $g = 0.85$  (empty square) and  $g = 0.95$  (full triangle). The vertical scale is logarithmic and  $\mu_s = 100\text{cm}^{-1}$ .

Monte Carlo simulations of the collection efficiencies through pinholes 1 and 4 (confocal paths) are well fitted with almost parallel straight lines (see Fig. 2 and correlation coefficient  $R^2 > 0.999$  in Table 1), in agreement with the exponential behavior expected for the collection efficiency with confocal modality. Note that the collection efficiency for the largest confocal pinhole is higher than that for the smallest one. In fact, depending on the pinhole diameter, more or less ballistic photons from the fluorescent focal volume are collected through the confocal pathway, but not any significant scattered photons. The slopes of the curves, or the apparent scattering and attenuation coefficients, range from about  $111.6$  to  $113.1\text{cm}^{-1}$  without absorption and from  $122.6$  to  $124.2\text{cm}^{-1}$  with absorption, depending on the size of the pinhole and of  $g$  (see Table 1). Note that the apparent coefficient is found systematically smaller for the smaller pinhole.

**Table 1. Slopes of the curves of Fig. 2 (in  $\text{cm}^{-1}$ ). The correlation coefficient  $R^2$  of the linear fit is shown in brackets. For pinholes 1 and 4, these values represent the apparent scattering coefficient  $\mu_s^{\text{app}}$  (or attenuation coefficient in the case of absorption), obtained directly from the collection efficiency  $\eta$ .**

	$\mu_s = 100\text{cm}^{-1}, \mu_a = 0$		$\mu_s = 100\text{cm}^{-1}, \mu_a = 10\text{cm}^{-1}$	
	$g = 0.85$	$g = 0.95$	$g = 0.85$	$g = 0.95$
Pinhole 1	112.4 (0.9999)	111.6 (0.9998)	123.3 (0.9999)	122.6 (0.9999)
Pinhole 4	113.1 (0.9999)	112.0 (0.9997)	124.2 (0.9999)	122.9 (0.9998)
NDS	5.7 (0.524)	0.7 (0.153)	19.0 (0.934)	13.0 (0.984)

This can be explained by the fact that when the pinhole diameter decreases, there is a decrease of the collection efficiency for the off-axis ballistic fluorescence photons originating from the PSF but outside the geometrical focal plane, although these photons strike the objective's front aperture. This effect promotes the collection of paraxial photons with shortest path lengths near to the imaging depth  $z_0$ , and then reduces the apparent attenuation coefficient. We then expect that the value of the apparent scattering coefficient found from our Monte Carlo simulations for the largest confocal pinhole ( $\mu_s^{\text{app}} = 113.1\text{cm}^{-1}$ ) will be closer to that obtained from a simple analytical model considering collection of the ballistic

photons only (see next section). It is also worthwhile to note that for confocal modality, similar results of the apparent scattering coefficient were obtained for different  $g$  within the range [0.80-0.98]. However, for  $g < 0.8$ , the axial profile of the NDS collection efficiency is not flat enough for considering  $\eta_{\text{NDS}}$  as constant within this relevant depth range. Moreover, for  $g \geq 0.99$  (peaked forward scattering), some scattered photons are not enough deflected to be rejected by the confocal pinhole. In that case, the apparent scattering coefficient decreases and its value depends on both values of  $g$  and  $\Phi_p$ .

In order to assess the validity of the method, we have calculated the confocal to non-descanned ratios. For the sake of clarity, we have only presented in Fig. 3 the ratios  $\eta_{\text{conf}}/\eta_{\text{NDS}}$  for pinhole 4, which is the pinhole used for the experiments (section 5).

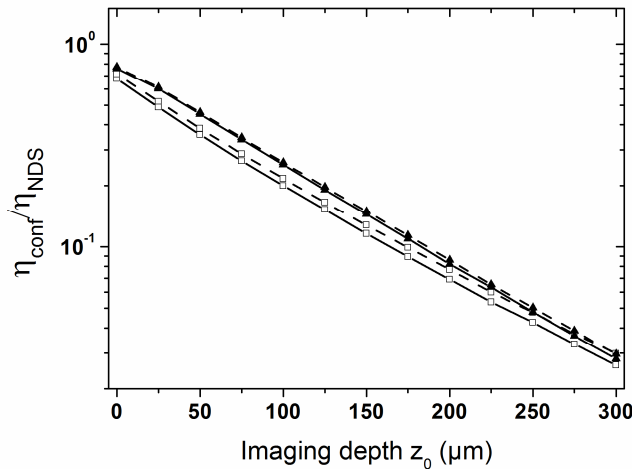


Fig. 3. Monte Carlo simulations of the  $z$ -profile of collection efficiencies ratio  $\eta_{\text{conf}}/\eta_{\text{NDS}}$  for pinhole 4, without absorption (full lines) and with absorption  $\mu_a = 10\text{cm}^{-1}$  (dashed lines), for  $g = 0.85$  (empty square) and  $g = 0.95$  (full triangle). The vertical scale is logarithmic.

Simulations demonstrate that the ratio is almost independent of  $\mu_a$  and  $g$ . Indeed, the slopes of the fitted curves, i.e. values of the apparent scattering coefficient, do not vary from more than 5% whatever the values of  $\mu_a$  and  $g$  (see Table 2).

**Table 2. Slopes of the curves of Fig. 3. The correlation coefficient  $R^2$  of the linear fit is shown in brackets. These values represent the apparent scattering coefficient  $\mu_s^{\text{app}}$ , obtained from the collection efficiency ratio  $\eta_{\text{conf}}/\eta_{\text{NDS}}$ , for pinhole 4.**

	$\mu_s = 100\text{cm}^{-1}, \mu_a = 0$		$\mu_s = 100\text{cm}^{-1}, \mu_a = 10\text{cm}^{-1}$	
	$g = 0.85$	$g = 0.95$	$g = 0.85$	$g = 0.95$
$\mu_s^{\text{app}} (\text{cm}^{-1})$	107.5 (0.9977)	111.2 (0.9998)	105.2 (0.9978)	109.9 (0.9998)

#### 4. Apparent scattering coefficient

In this section, we introduce a simple model to derive the true scattering coefficient  $\mu_s$  from the measured apparent one  $\mu_s^{\text{app}}$ . In this simple model, we assumed that only ballistic photons emitted from the geometrical focus at depth  $z_0$  beneath the scattering sample surface are epically collected by the objective lens. The detected intensity  $I(z_0, \mu_s)$  was then calculated by averaging the unscattered intensity transmitted by the medium over the solid angle of the collecting objective.  $I_0$  being the overall fluorescence intensity emitted over  $4\pi$  sr from the geometrical focus, the collection efficiency for the ballistic intensity can be written as:



$$\eta_{bal}(z_0, \mu_s) = \frac{I(z_0, \mu_s)}{I_0} = \frac{1}{2} \int_1^{CA^{-1}} \frac{\exp(-\mu_s z_0 u)}{u^2} du \quad (3)$$

where  $u = 1/\cos\theta$  and  $CA = \cos\theta_{NA}$ . The factor  $\exp(-\mu_s z_0/\cos\theta)$  in Eq. (3) is the probability for a photon not to be scattered when it propagates through the turbid medium with an angle  $\theta$  from the optical axis. When  $\mu_s z_0 \rightarrow 0$ ,  $\eta_{bal}$  reduces to  $\eta_0 = (1 - \cos\theta_{NA})/2$ , which corresponds to the collection efficiency either without scattering ( $\mu_s \rightarrow 0$ ) or at zero depth ( $z_0 \rightarrow 0$ ).

Since Monte Carlo simulations showed that the collection efficiency in the confocal mode scales like  $\exp(-\mu_s^{app} z_0)$ , we performed a numerical integration of Eq. (3) over the aperture of the objective lens used in our experiments (0.9-NA water immersion objective,  $CA = \cos[\arcsin(NA/n)] = 0.7363$ ), for different products  $\mu_s z_0$ . The results are represented as a function of  $z_0$  in Fig. 4(a), for various  $\mu_s$ . Data points are well fitted by first order polynomials for imaging depths  $z_0$  comprised in the interval  $[0-300\mu m]$ , and  $\mu_s$  varying from 10 to  $250\text{cm}^{-1}$  (correlation coefficient  $R^2 > 0.9999$ ). The slopes of the fits provide an apparent scattering coefficient  $\mu_s^{app}$  which is represented as a function of  $\mu_s$  in Fig. 4(b). As expected, we find  $\mu_s^{app} > \mu_s$ , since all the photon paths are either larger or equal to  $z_0$ . In addition, the difference between  $\mu_s^{app}$  and  $\mu_s$  increases as  $\mu_s$  increases. Note that when  $\mu_s \approx 100\text{cm}^{-1}$  the curve of Fig. 4(b) provides  $\mu_s^{app} \approx 114.5\text{cm}^{-1}$ , which is in good agreement with the value obtained from Monte Carlo simulation, especially for the largest confocal pinhole ( $\mu_s^{app} \approx 113.1\text{cm}^{-1}$  for  $g = 0.95$ , see Table 1).

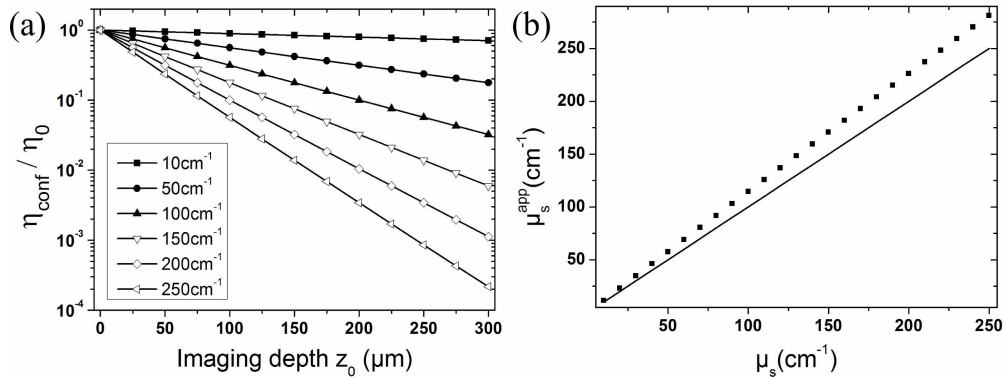


Fig. 4. (a) Epi-collection efficiencies for the ballistic fluorescence photons produced by two-photon excitation at focus of a water immersion objective with  $NA = 0.9$ , as a function of the imaging depth  $z_0$  in a turbid medium with various scattering coefficients. Dots were obtained from numerical integration of Eq. (3) whereas full lines are the corresponding linear regressions. (b) apparent scattering coefficient  $\mu_s^{app}$  derived from curve fitting of Fig. 4(a) as function of the true scattering coefficient  $\mu_s$ . The full line is a guide for the eye (bisector).

Moreover using Taylor-series developments and least squares methods, we found that  $\mu_s$  can be well approximated from  $\mu_s^{app}$  using the following relationship:

$$\mu_s^{corr} = \frac{2A\mu_s^{app}}{1 + \sqrt{1 - 2\mu_s^{app} z_{corr} B}} \quad (4)$$

where  $A = [CA - 1]/\ln CA$ ,  $B = [A^2/CA] - 1$ ,  $z_{corr} = [\langle z_0^3 \rangle - \langle z_0 \rangle \langle z_0^2 \rangle] / [\langle z_0^2 \rangle - \langle z_0 \rangle^2]$  with  $\langle z_0^n \rangle = \sum_p \langle z_{0p}^n \rangle / N$ , where  $N$  is the number of depth values  $z_{0p}$  which are considered for fitting the data (from 0 to  $300\mu m$  by  $25\mu m$  step). Here,  $\mu_s^{corr}$  stands for the corrected scattering coefficient, calculated from Eq. (4). For the objective lens and axial steps used in our experiment, we obtained  $A \approx 0.8614$ ,  $B \approx 7.836 \cdot 10^{-3}$ , and  $z_{corr} = 300\mu m$ . Using these parameters in Eq. (4), we recovered  $\mu_s^{corr} \approx 100\text{cm}^{-1}$  from the previous value  $\mu_s^{app} \approx 114.5\text{cm}^{-1}$ . It is

worthwhile to note that because  $B \ll 1$ ,  $\mu_s^{\text{corr}} \approx A \cdot \mu_s^{\text{app}}$  for small depths  $z_0$  of the order of  $1/\mu_s$ . Note that this simplified expression can be easily recovered by considering a first-order development of  $\exp(-\mu_s z_0)$  in Eq. (3). The corrected scattering coefficients  $\mu_s^{\text{corr}}$  recalculated from Eq. (4) are plotted as a function of the starting values of  $\mu_s$  in Fig. 5(a). As can be seen, the recalculated points almost superimpose the bisector. The relative error is plotted in Fig. 5(b), indicating a good agreement with discrepancies of the order of 0.3% for  $\mu_s$  as large as  $250\text{cm}^{-1}$ .

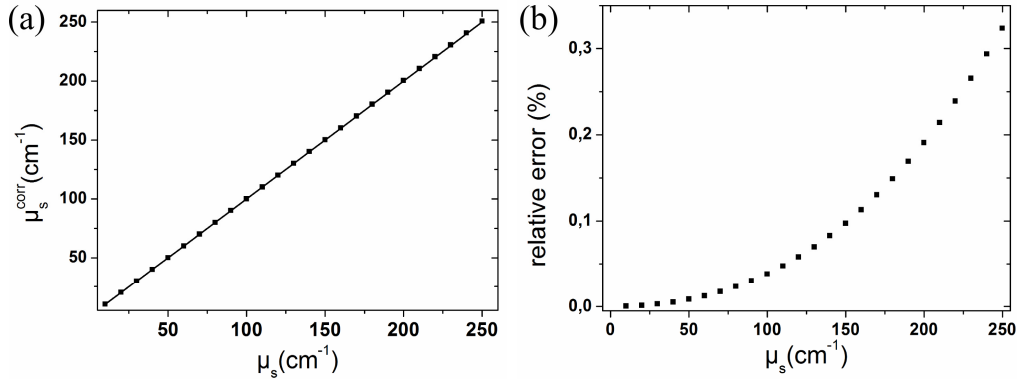


Fig. 5. (a) Corrected scattering coefficient  $\mu_s^{\text{corr}}$  from Eq. (4) versus true scattering coefficient  $\mu_s$ ; (b) Relative error between  $\mu_s^{\text{corr}}$  and  $\mu_s$ .

Table 3 shows the corrected scattering coefficients derived from the apparent ones obtained from Monte Carlo simulations for a scattering medium with  $\mu_s = 100\text{cm}^{-1}$ .

**Table 3. Corrected scattering coefficient  $\mu_s^{\text{corr}}$  from the apparent scattering coefficients  $\mu_s^{\text{app}}$  obtained from Monte Carlo simulations for a scattering medium with  $\mu_s = 100\text{cm}^{-1}$  (see Table 2).**

	$\mu_a = 0$		$\mu_a = 10\text{cm}^{-1}$	
	$g = 0.85$	$g = 0.95$	$g = 0.85$	$g = 0.95$
$\mu_s^{\text{corr}} (\text{cm}^{-1})$	93.8	97.1	91.8	95.9

Thus for a limited range of imaging depths and with well-known and well-chosen objective parameters, measuring the confocal-to-NDS fluorescence intensity ratio on a two-photon microscope enables to retrieve the true scattering coefficient of a turbid medium, with accuracy better than 10%, almost independently of the anisotropy factor, the absorption coefficient or the size of the confocal pinhole (comparing values of  $\mu_s^{\text{app}}$  in Table 1 for pinholes 1 and 4).

## 5. Materials

### 5.1 Two-photon microscope

A two-photon excitation fluorescence microscope based on an infrared (IR) coated confocal microscope (FV300/BX51WI, Olympus France, Rungis) and a femtosecond Ti:Sapphire laser (Verdi-V5/Mira, Coherent France, les Ulis) tuned at  $\lambda = 830\text{nm}$  were used in this study (pulse duration  $\sim 200\text{fs}$ ). A home-built NDS port was mounted abreast of the fluorescence cube turret, on the left side of the microscope, in association with a home-built cube containing a dichroic mirror (675DCXRU, Chroma, Brattleboro, USA) and a high aperture collection lens [6]. The external photomultiplier tube (PMT) module (H7710-13, Hamamatsu Photonics France, Massy) of the NDS port was connected to a transimpedance amplifier (C7319,

Hamamatsu Photonics France, Massy) in order to fit the internal PMT of the DS port and use the full range of the electronics and software of the confocal microscope. IR blocking filters (Schott BG39 model, Edmund Optics Europe, York, UK) were inserted on both the DS and NDS pathways. A long working distance objective lens (LUMPlanFl 60 × /0.90W, Olympus France, Rungis) was water-coupled to the phantoms.

## 5.2 Optical phantoms

Experiments were carried out on tissue mimicking scattering phantoms based on polystyrene microspheres in aqueous agarose gels. More precisely polystyrene microspheres (Polysciences Inc., USA) of various diameters were embedded in a 4% agarose gel matrix (Sigma-Aldrich Co., USA). In order to produce two-photon excitation fluorescence, a water-diluted solution of sulforhodamine B (Kiton Red 620<sup>®</sup>, Exciton, USA) was added to the gel at a final concentration of about 20μM. Laser excitation wavelength was set at 830nm to fit with the maximum of two-photon cross-section of Kiton Red 620<sup>®</sup> [16]. The maximum of the fluorescence spectrum measured from the labelled gels was obtained for a wavelength  $\lambda_{\text{max}}$  of ~600nm (FWMH~30nm). This value was then applied as the collection wavelength in all our simulations and measurements. The emission peak was assumed narrow enough (FWMH/ $\lambda_{\text{max}}$ ~5%) to consider  $\mu_s(\lambda_{\text{max}})$  and the inherently wavelength-averaged experimental  $\mu_s$  in good agreement. The refractive indices of agarose gels  $n_a$  and polystyrene spheres  $n_s$  for this wavelength were respectively fixed to  $n_a \approx n_{\text{water}} = 1.33$  [17,18] and  $n_s = 1.59$  [19]. Bead concentrations were calculated from Wu and Wang's code [3] based on Mie theory in order to obtain scattering coefficients of 50cm<sup>-1</sup> and 100cm<sup>-1</sup> at 600nm. Bead diameters of 0.54μm, 1.53μm and 4.52μm were selected for this study, resulting in anisotropy factors  $g$  of respectively 0.85, 0.93 and 0.87 which are typical of biological tissues in which forward scattering prevails [20]. Table 4 summarizes the properties of the tissue phantoms.

**Table 4. Microsphere diameters and concentrations, and resulting scattering properties of agarose gels used as tissue-mimicking samples. Error bars were estimated from the uncertainty on volumes taken from stock solutions of microbeads.**

Bead diameter (μm)	Anisotropy factor $g$	Concentration (beads.cm <sup>-3</sup> )	Scattering coefficient at $\lambda = 600\text{nm}$ (cm <sup>-1</sup> )
0.54	0.85	$(5.4 \pm 0.3) \times 10^{10}$	$100.0 \pm 6.5$
		$(2.7 \pm 0.2) \times 10^{10}$	$50.0 \pm 3.4$
1.53	0.93	$(1.5 \pm 0.1) \times 10^9$	$100.0 \pm 6.7$
		$(7.6 \pm 0.4) \times 10^8$	$50.0 \pm 2.4$
4.52	0.87	$(2.4 \pm 0.1) \times 10^8$	$100.0 \pm 6.1$
		$(1.2 \pm 0.8) \times 10^8$	$50.0 \pm 3.2$

Custom ~1cm<sup>3</sup>-cylindrical wells were drilled in a PMMA plate and coverslips were glued on the top to obtain an optical quality interface. Before polymerization of agarose, the mixtures were injected within the wells through small ducts drilled on the bottom of the plate, then sealed to prevent evaporation. The mixtures were further used to load rectangle glass capillaries of inner thickness from 100 to 600μm with a step size of 100μm (CM Scientific Ltd., Silsden, UK). These allowed us to evaluate independently the scattering coefficients from a simple collimated transmission experiment [3]. Abreast and superposed gels of distinct scattering coefficients were also prepared to determine if our technique was able to reveal lateral and axial (in-depth) heterogeneities of the scattering coefficient.

## 6. Experimental results

As previously explained, our method is based on the measurement of the confocal-to-NDS fluorescence intensity ratios of a two-photon microscope as a function of imaging depth. In order to optimize the signal-to-noise ratio while avoiding photobleaching, intensity measurements were averaged on a small area of the gels rather than at fixed points. Z-stacks

of zoomed images were then acquired over a depth range for which the NDS collection efficiency of the microscope can be considered constant (i.e.  $320\mu\text{m}$ , corresponding to the field of view of the NDS port). Zooming allowed reduction of the scan angle which provides experimental conditions close to those of the simulations where the fluorescence source was considered on the optical axis. To further improve the signal-to-noise ratio, images were averaged over two scans using Kalman filtering. Laser power at the objective was determined at the beginning of the experiment for maximizing TPEF intensity near the sample surface while avoiding photobleaching. The PMT supplied voltages were also set at first to exploit the full 12-bit intensity resolution of the microscope.

The six wells filled with the scattering gels prepared as described above were imaged from the surface to the bottom with an axial step size of  $10\mu\text{m}$ . Imaging was performed successively through the DS port (confocal) equipped with the pinhole 4 (diameter  $200\mu\text{m}$ ) and the NDS port. The overall acquisition time of a complete image stack was less than one minute. For gels with scattering coefficient of  $100\text{cm}^{-1}$ , the signal-to-noise ratio was not high enough with confocal modality to obtain reliable measurements beyond a depth of about  $200\mu\text{m}$ . The mean intensity value of the  $256 \times 256$  pixels<sup>2</sup> images after background subtraction was calculated using ImageJ (NIH freeware, Measure Stacks plugin) and considered as a measure of the TPEF signal. Figure 6 is a semi-log representation of the measured confocal-to-NDS intensity ratios as a function of depth for the six wells. Linear fitting of the experimental data (straight lines), excluding the first  $30\mu\text{m}$  close to the sample surface for which measurements were not reliable, provides the actual scattering coefficient from the apparent one according to the model of section 4. The collimated transmission method was implemented in parallel on a series of 100 to  $600\mu\text{m}$ -thick capillaries loaded with the same scattering gels, using a 633nm He-Ne laser as a source. A series of capillaries loaded with clear fluorescent gels was used as reference to correct measurements for residual optical losses due to absorption of the dye and Fresnel reflections. The results are summarized in Table 5. Although some differences with anticipated values exist, the scattering coefficients derived from the two methods are in excellent agreement if one takes into account measurement uncertainties. Moreover, as expected, the results appear independent of the anisotropy factor  $g$  (0.85 to 0.93 see Table 4). This clearly demonstrates the relevance of our new approach.

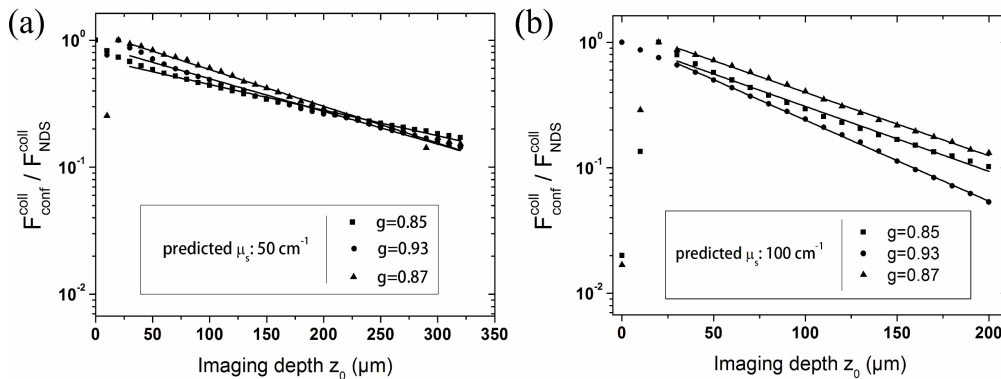
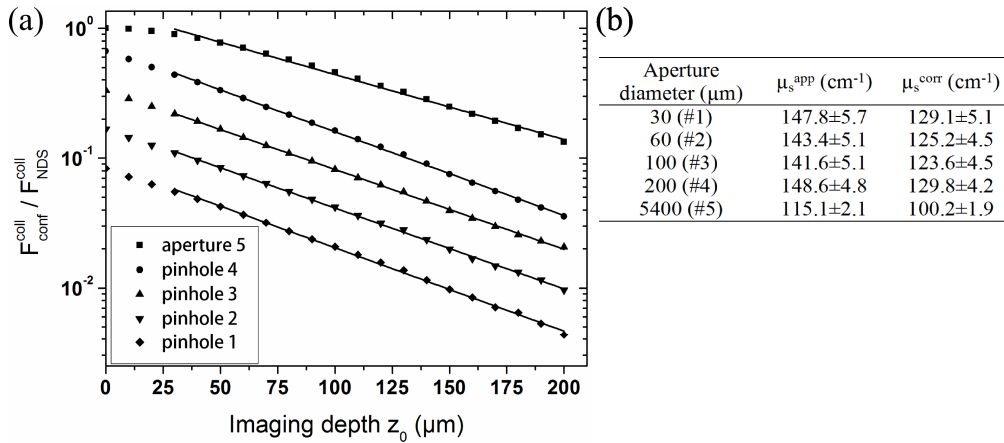


Fig. 6. Semi-log representation of the confocal-to-nondescanned ratios of the two-photon excitation fluorescence intensity versus imaging depth measured from six scattering gels with scattering coefficients of  $\sim 50\text{cm}^{-1}$  and  $\sim 100\text{cm}^{-1}$ , and three distinct anisotropy factors (see Table 4). The confocal pinhole has a diameter of  $200\mu\text{m}$  (pinhole 4). Straight lines stand for linear fits of experimental data (dots), allowing to determine the true scattering coefficients through Eq. (4).

**Table 5. Scattering coefficients of agarose gel mixtures for three bead diameters, i.e. three different anisotropy factors  $g$ . The scattering coefficients are from left to right: the scattering coefficient anticipated from Mie theory ( $\mu_s^{\text{ant}}$ ), the apparent coefficient derived from the confocal-to-NDS ratio ( $\mu_s^{\text{app}}$ ), the corresponding scattering coefficient as obtained after correction ( $\mu_s^{\text{corr}}$ ) and the ones obtained from the collimated transmission method ( $\mu_s^{\text{trans}}$ ). Errors bars on the experimental scattering coefficients were obtained from statistics on two-photon images and from repetitive measurements for the collimated method.**

Beads diameter ( $\mu\text{m}$ )	Anisotropy factor $g$	$\mu_s^{\text{ant}}$ ( $\text{cm}^{-1}$ )	$\mu_s^{\text{app}}$ ( $\text{cm}^{-1}$ )	$\mu_s^{\text{corr}}$ ( $\text{cm}^{-1}$ )	$\mu_s^{\text{trans}}$ ( $\text{cm}^{-1}$ )
0.54	0.85	$50.0 \pm 3.4$	$46.4 \pm 3.5$	$40.2 \pm 3.0$	$40.2 \pm 2.9$
		$100.0 \pm 6.5$	$119.1 \pm 2.0$	$103.7 \pm 1.8$	$99.8 \pm 4.3$
1.53	0.93	$50.0 \pm 2.4$	$59.3 \pm 1.4$	$51.5 \pm 1.2$	$51.7 \pm 4.1$
		$100.0 \pm 6.7$	$148.6 \pm 4.8$	$129.8 \pm 4.2$	$131.7 \pm 6.1$
4.52	0.87	$50.0 \pm 3.2$	$66.6 \pm 3.5$	$57.9 \pm 3.1$	$59.9 \pm 2.8$
		$100.0 \pm 6.1$	$116.2 \pm 7.3$	$101.2 \pm 6.5$	$105.6 \pm 5.4$

We have also evaluated the robustness of our method with respect to the size of the pinhole. The confocal-to-NDS ratio measured as a function of the imaging depth for the four confocal pinholes and a fifth aperture, much larger than the others, are represented in Fig. 7. Note that this aperture was obtained by removing the fifth pinhole of the confocal wheel so as to allow two-photon imaging modality via the DS port.



**Fig. 7. (a)** Confocal-to-NDS fluorescence intensity ratios as a function of the imaging depth inside a  $\sim 130\text{cm}^{-1}$  scattering gel containing polystyrene beads of  $1.53\mu\text{m}$  in diameter ( $g = 0.93$ ), for the four confocal pinholes of our scanning microscope and a much larger aperture. **(b)** Table reporting the apparent and corrected scattering coefficient for the five apertures.

Experimental data are again well fitted by first order polynomials which are almost parallel each other. Consequently, apparent and corrected scattering coefficients, as summarized in Table 4, appear independent of the diameter of the confocal pinhole, all uncertainties included, in accordance with Monte Carlo simulations of section 3. Obtaining a higher scattering coefficient ( $\sim 130\text{cm}^{-1}$ ) than the one expected ( $100\text{cm}^{-1}$ ) may be explained by experimental uncertainties on the volumes taken both from the stock solution of microbeads and from the agarose solution. The lower value of  $\sim 100\text{cm}^{-1}$  found with the larger aperture #5 can be accounted for Monte Carlo simulation. Indeed, a larger aperture allows scattered photons to be detected, resulting in a decrease of the apparent scattering coefficient. This effect is quite similar to the decrease observed for  $g$  values above 0.99 (see section 3).

Finally, we performed measurements on biomimetic samples consisting of two distinct scattering gels either one above the other (superimposed) or one beside the other (juxtaposed). For the superimposed sample, a  $\sim 100\text{cm}^{-1}$  scattering gel containing beads of  $4.52\mu\text{m}$  in diameter was extracted from a  $100\mu\text{m}$  inner thickness capillary and deposited on a microscope coverslip. A  $\sim 200\text{cm}^{-1}$  scattering gel with  $0.54\mu\text{m}$  beads was laid down on the first, and the whole sample was deposited on a microscope slide. An example of TPEF images of the two superimposed gels is given in insertion of Fig. 8(a); we can see on the left image that large polystyrene beads included in the top gel are resolved. In that case, the confocal-to-NDS fluorescence intensity ratio is expected to scale like  $\exp(-\mu_{s1}^{\text{app}} \cdot z_0)$  for  $z_0 < t_1$ , and like  $\exp[(\mu_{s2}^{\text{app}} - \mu_{s1}^{\text{app}}) \cdot t_1] \exp(-\mu_{s2}^{\text{app}} \cdot z_0)$  for  $z_0 > t_1$ . Here,  $\mu_{s1}^{\text{app}}$  and  $\mu_{s2}^{\text{app}}$  are the apparent scattering coefficients or the slopes of semi-log representation of the experimental fluorescence ratio as a function of the imaging depth  $z_0$  for the first (top) and the second (bottom) gels, whereas  $t_1$  is the thickness of the first one. The same experimental method as previously described was used, except that the imaging depth was limited to  $150\mu\text{m}$  due to the high scattering coefficient of the bottom gel. The axial profile of the confocal-to-NDS fluorescence ratio reported in Fig. 8(a) well reveals a sharp break of the slope at a depth of about  $80\mu\text{m}$  due to the transition from one medium to the other, with a fair exponential behavior as shown by the straight line fitting of the data in this semi-log representation. The corresponding apparent and corrected scattering coefficients are summarized in the table of Fig. 8(b). Higher values compared to those expected ( $100$  and  $200\text{cm}^{-1}$ ) may be explained by a dehydration of the gels during the preparation stage of the assembly.

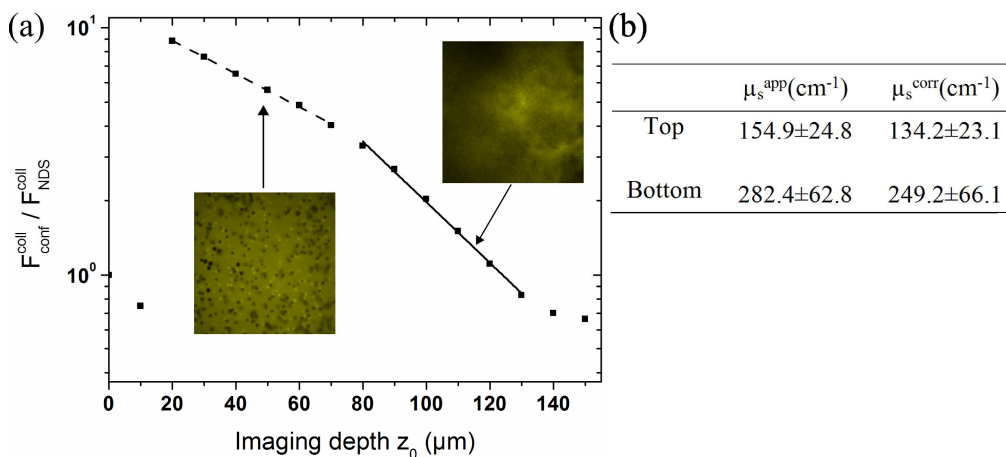


Fig. 8. (a) Intensities ratios versus imaging depth in the case of superposed gels with different scattering properties. Points represent the experimental data. Dash line is the fit of the ratio for the top gel, and continuous line for the bottom gel. Inserts are  $\sim 50 \times 50\mu\text{m}^2$  images of the gels through the NDS pathway (left:  $4.52\mu\text{m}$  beads top layer imaged at  $30\mu\text{m}$  depth, right:  $0.54\mu\text{m}$  beads bottom layer imaged at  $90\mu\text{m}$  depth). (b) Table reporting the apparent and corrected scattering coefficient of the two layers.

For the juxtaposed gels, the two samples were prepared in  $500\mu\text{m}$ -width glass capillaries which were carefully broken to extract and laid down the gels side-by-side between a microscope slide and a coverslip. In order to map the scattering coefficient, z-stacks ( $300\mu\text{m}$  in-depth with a step size of  $5\mu\text{m}$ ) of 5-fold zoomed images ( $\sim 50 \times 50\mu\text{m}^2$ ) of the area close to the interface between the gels were acquired at a definition of  $2048 \times 2048$  pixels<sup>2</sup> (see Fig. 9(a)). Each image of the stack was segmented into 4096 ( $64 \times 64$ ) small areas. For all these areas we evaluated the apparent scattering coefficient from linear fitting of the corresponding axial profiles of the confocal-to-NDS fluorescence ratio. Areas whose fit had a  $R^2$  value less than 0.9 were excluded (14/4096). A  $64 \times 64$  map of the scattering coefficient (in a gray scale) obtained near the interface of the gels is reported in Fig. 9(b). Both gels are clearly

distinguished by their scattering coefficients. Furthermore an intermediate region is visible at the interface, which can be due to the fact that when the fluorescent source is deeply localized near the interface, photons can cross the two scattering media prior to be collected by the high-NA objective. The histogram corresponding to  $\mu_s$  values of Fig. 9(b) exhibits two peaks around 250 and 625  $\text{cm}^{-1}$  and intermediate values reflecting the interfacial effect (cf. Fig. 9(c)). Figure 9(d) is a histogram of the  $R^2$  value of the linear fits used to recover the apparent scattering coefficient from each block of the image, demonstrating the robustness of our method.

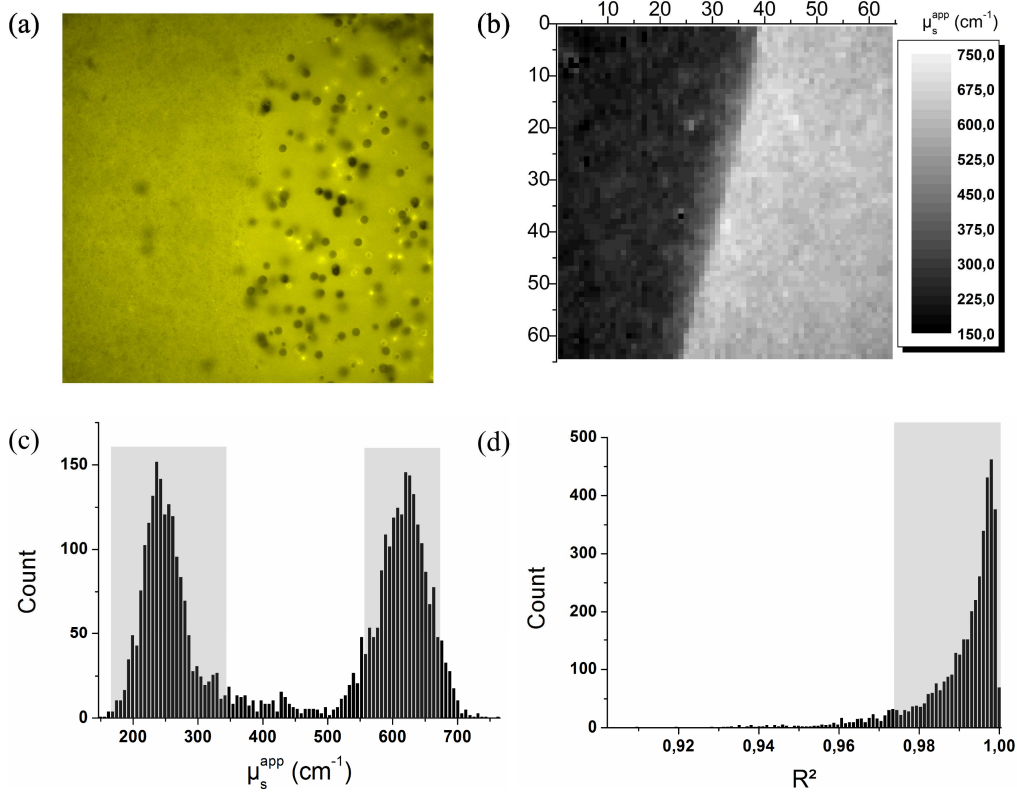


Fig. 9. Scattering coefficient imaging of two abreast gels. The left part is a 0.54  $\mu\text{m}$  beads gel with low  $\mu_s$ , and the right part is a 4.52  $\mu\text{m}$  beads gel with high  $\mu_s$ . (a)  $\sim 50 \times 50 \mu\text{m}^2$  image of the sample through the NDS pathway, for an imaging depth of 30  $\mu\text{m}$ . (b) Reconstructed scattering coefficient map. (c) Histogram of  $\mu_s^{\text{app}}$ . (d) Histogram of the correlation coefficient  $R^2$ . Note that 90% of the data are included within the grey areas.

## 7. Conclusion

We have reported an original and simple method to measure the scattering coefficient of turbid media from the intensity ratio of the fluorescence signals epi-collected through the confocal and the NDS ports of a scanning two-photon microscope. We have shown from Monte Carlo simulations that this ratio is almost independent of the absorption, of the scattering anisotropy of the medium, for  $g$  values in the range [0.8-0.99], and of the size of the confocal pinhole. Moreover our method overcomes the problem of the unknown excitation function of the microscope. By measuring the axial profile of the confocal-to-NDS fluorescence ratio, we have been able to retrieve the scattering coefficient according to a simple ballistic model of the light collection by a high-NA objective lens. The method has been validated on optical phantoms consisting of polystyrene microspheres embedded in aqueous agarose gels. Comparison of the results with a collimated transmission method

clearly demonstrated the relevance of our approach. Finally we showed that our technique enables to separate two scattering media, either juxtaposed or superimposed, from their scattering coefficients. This paves the way for a new imaging method of the scattering coefficient of biological samples that could be used for biomedical diagnosis.

### **Acknowledgments**

Authors acknowledge S. Hernot for her precious help during the fabrication of the scattering gels. D. Sevrain is supported by the Ministère de l'Enseignement Supérieur et de la Recherche.